Supplementary Materials

Magnetic anisotropic pinning and symmetry breaking in ruthenate superlattices

Zhongyuan Jiang[1,#], Zhiwei Zhang[2,#], Kesen Zhao[3,#], Wenjie Meng[3], Yuanyuan Zhao[2], Yubin Hou[3], Zhangzhang Cui[1], Jian Zhang[1], Zheling Shan[1], Haoliang Huang[2], Qingyou Lu[1,3], Yalin Lu[1]

[1]Hefei National Laboratory, Anhui Laboratory of Advanced Photon Science and Technology, Hefei National Laboratory for Physical Sciences at the Microscale, University of Science and Technology of China, Hefei 230026, Anhui, China.
[2]Quantum Science Center of Guangdong-Hong Kong-Macao Greater Bay Area, Shenzhen 518045, Guangdong, China.
[3]Anhui Province Key Laboratory of Condensed Matter Physics at Extreme Conditions, High Magnetic Field Laboratory, Chinese Academy of Sciences, Hefei 230031, Anhui, China.
[#]These authors contributed equally to this work.

Correspondence to: Dr. Haoliang Huang, Quantum Science Center of Guangdong-Hong Kong-Macao Greater Bay Area, Shenzhen 518045, Guangdong, China. E-mail: huanghaoliang@quantumsc.cn; Pro. Qingyou Lu, Anhui Province Key Laboratory of Condensed Matter Physics at Extreme Conditions, High Magnetic Field Laboratory, Chinese Academy of Sciences, Hefei 230031, Anhui, China. E-mail: qxl@ustc.edu.cn; Prof. Yalin Lu, Hefei National Laboratory, Anhui Laboratory of Advanced Photon Science and Technology, Hefei National Laboratory for Physical Sciences at the Microscale, University of Science and Technology of China, Hefei 230026, Anhui, China. E-mail: yllu@ustc.edu.cn

ORCID: Haoliang Huang (0000-0002-5686-5519), Qingyou Lu (0000-0003-1934-8165), Yalin (0000-0001-8240-5404)

RSM Data and strain scenario for all samples

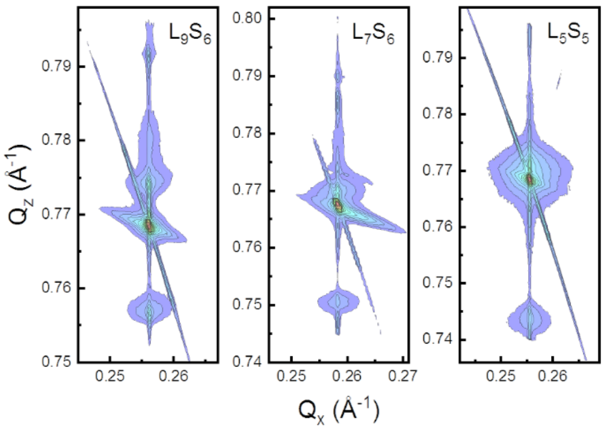

Supplementary Figure 1. RSM for all the superlattice samples. Equal in-plane Q values for each respective sample indicate completely coherent growth of all the superlattices on STO substrate.

MFM images for the L_9S_6 sample

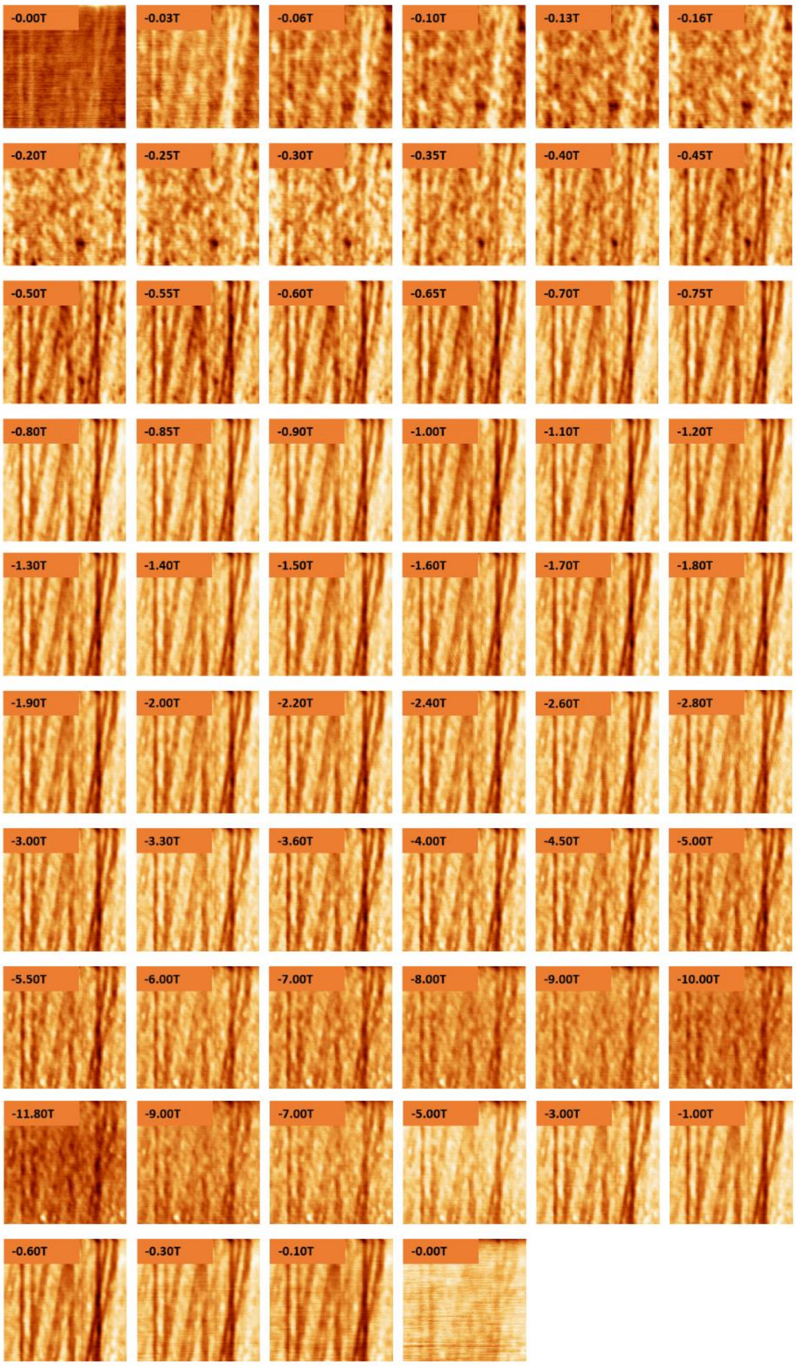

Supplementary Figure 2. Out-of-plane field-dependent loop scan (0 to −11.80 T to 0) at 75 K.

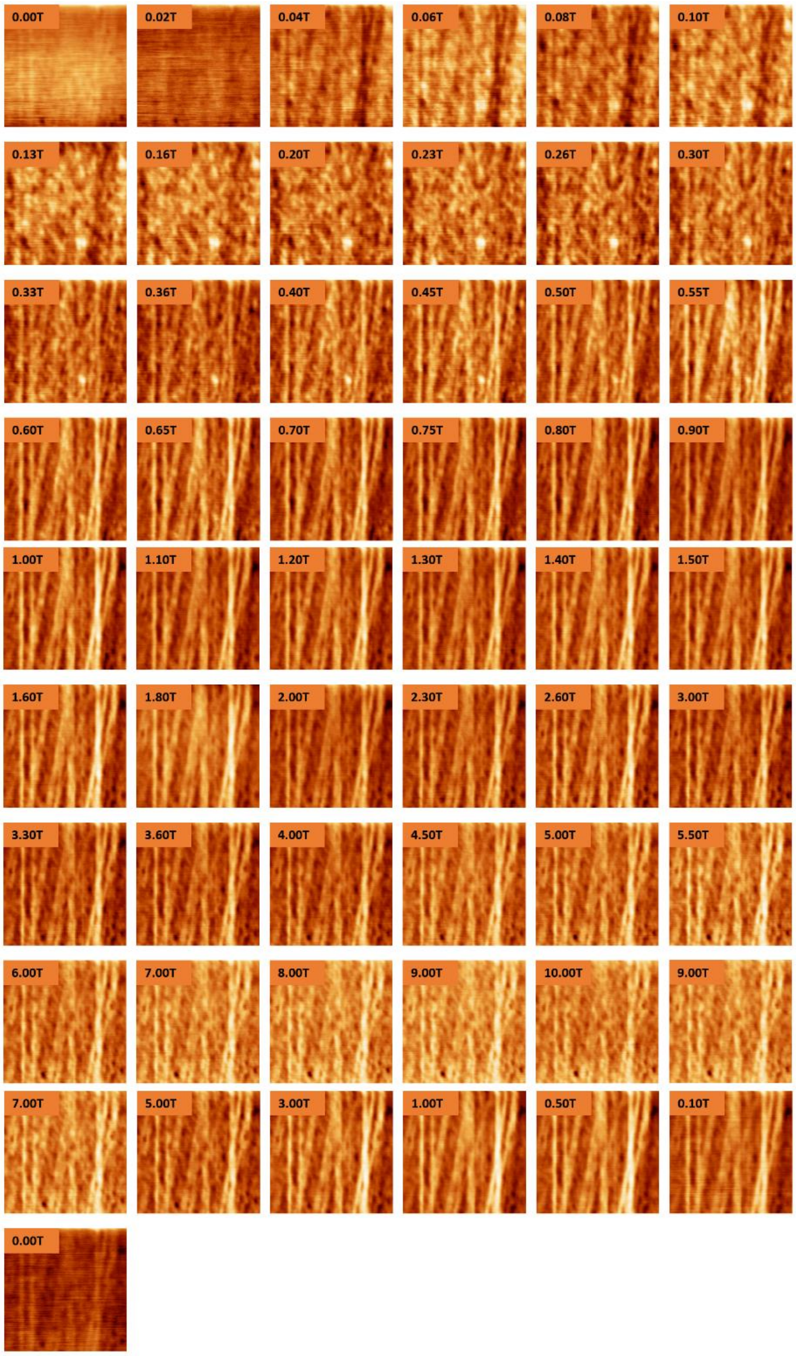

Supplementary Figure 3. Out-of-plane field-dependent loop scan (0 to 10.00 T to 0) at 75 K.

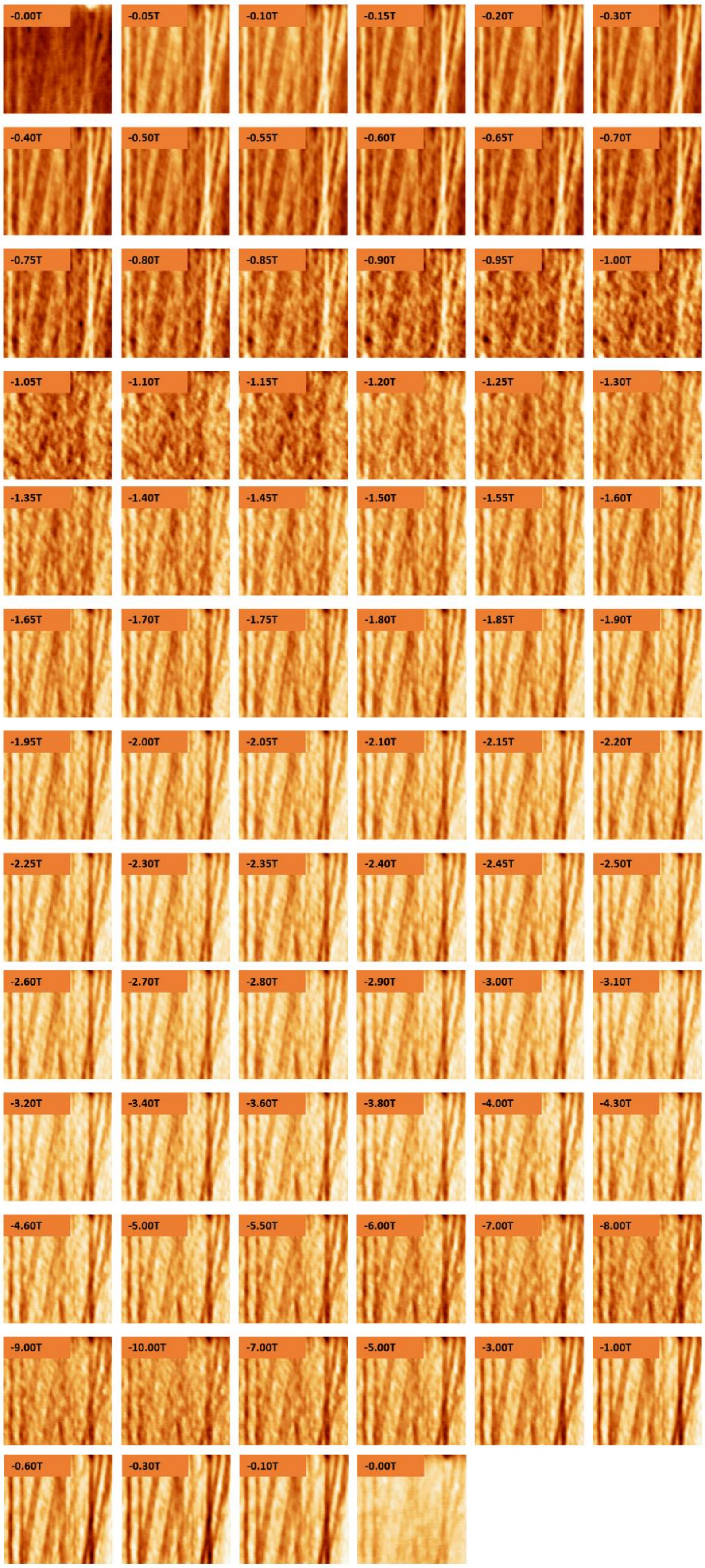

Supplementary Figure 4. Out-of-plane field-dependent loop scan (0 to −10.00 T to 0) at 25 K.

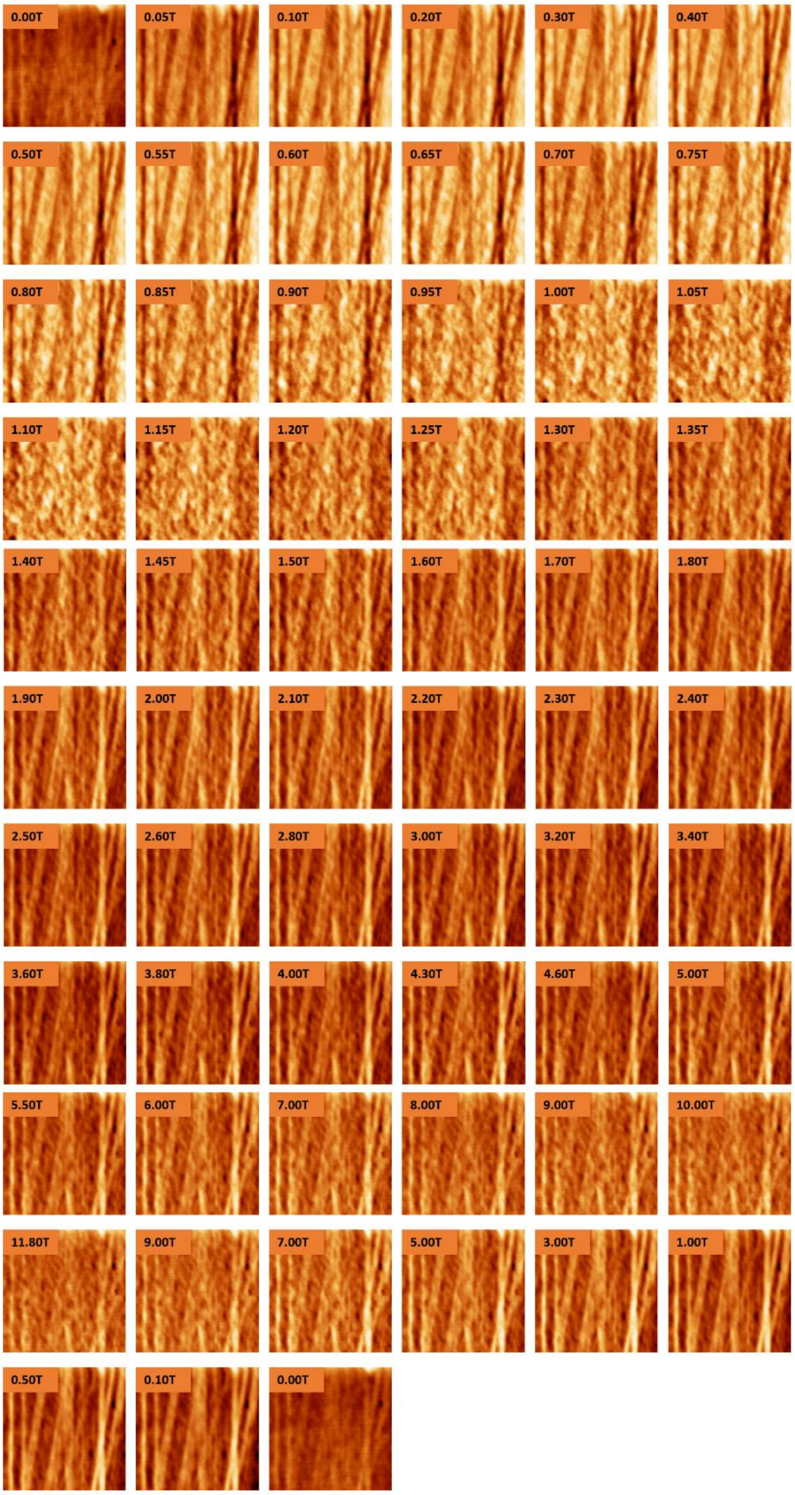

Supplementary Figure 5. Out-of-plane field-dependent loop scan (0 to 11.80 T to 0) at 25 K.

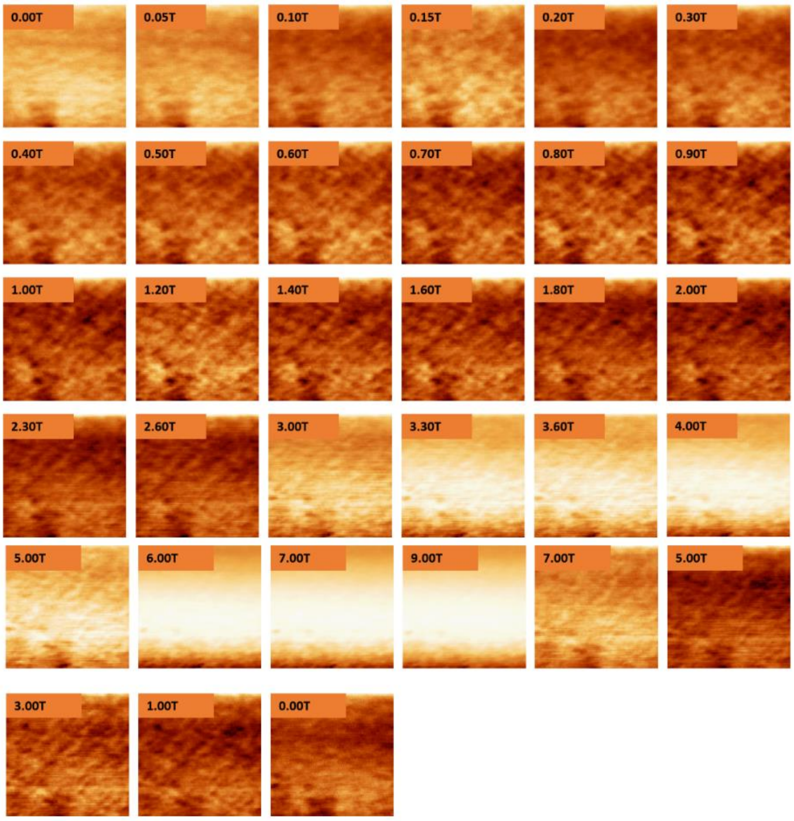

Supplementary Figure 6. In-plane field-dependent loop scan (0 to 9.00 T to 0) at 75 K.

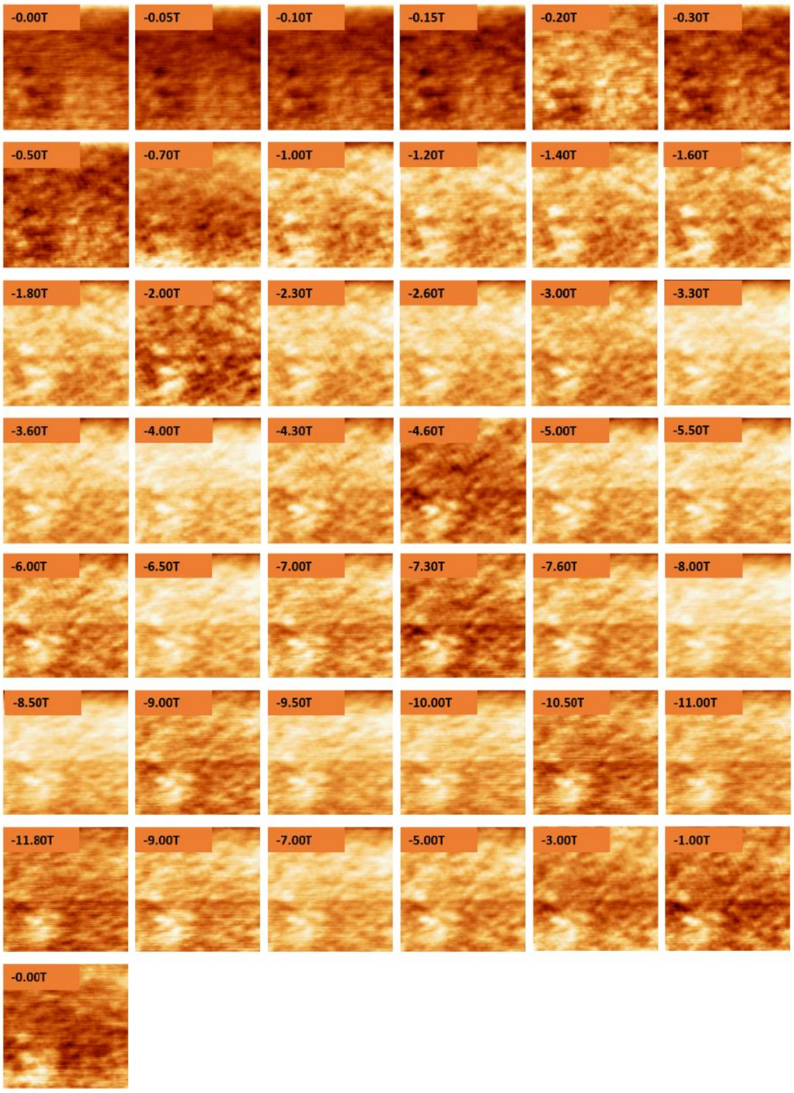

Supplementary Figure 7. In-plane field-dependent loop scan (0 to −11.80 T to 0) at 25 K.

MAR data and fitting for the L_9S_6 sample

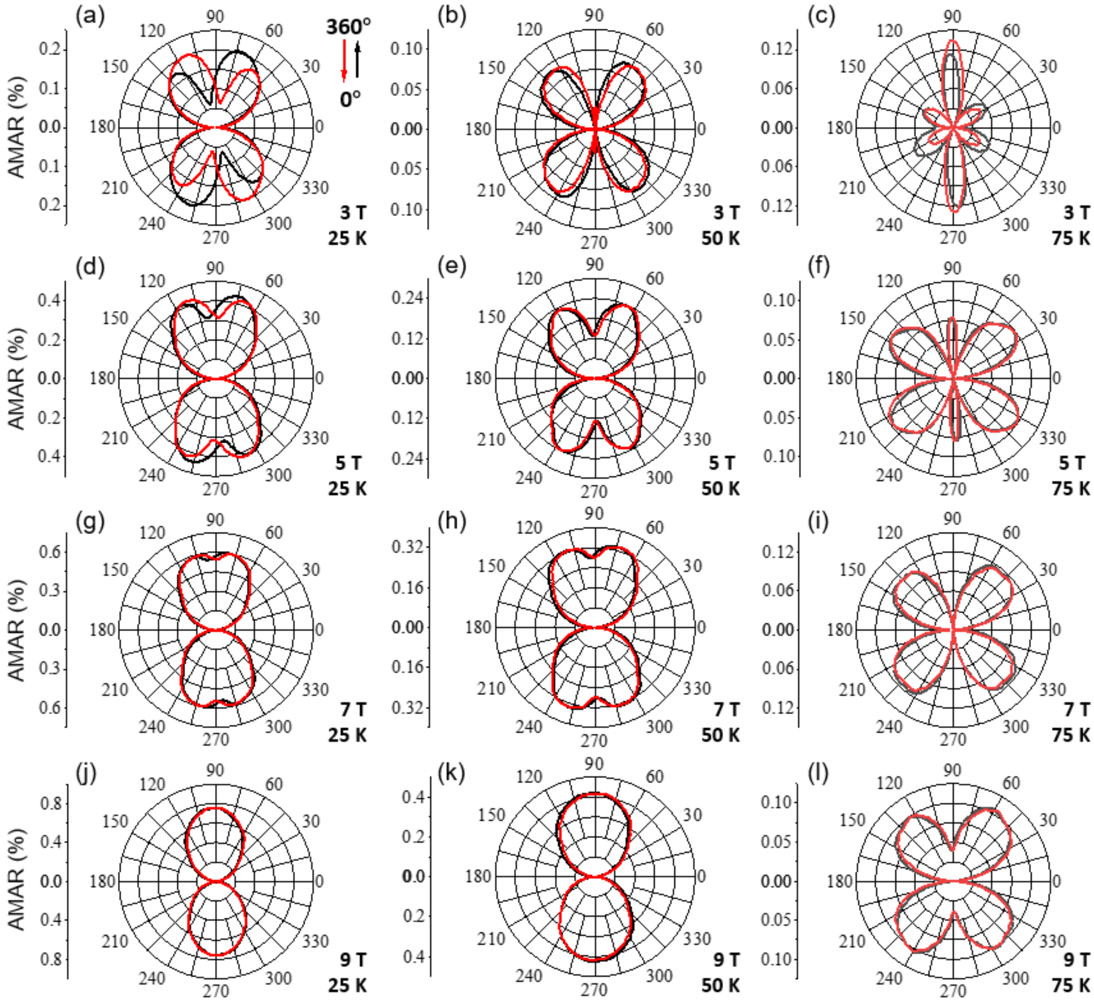

Supplementary Figure 8. MAR magnitude butterfly plots of L_9S_6 superlattice. The radial axis represents the MAR magnitude in percentage. Red curves show data acquired during counter-clockwise field rotation (360° → 0°), while black curves represent clockwise rotation (0° → 360°). (a–c) MAR magnitude at 3 T for 25 K, 50 K, and 75 K, respectively. (d–f) MAR magnitude at 5 T for 25 K, 50 K, and 75 K, respectively. (g–i) MAR magnitude at 7 T for 25 K, 50 K, and 75 K, respectively. (j–l) MAR magnitude at 9 T for 25 K, 50 K, and 75 K, respectively.

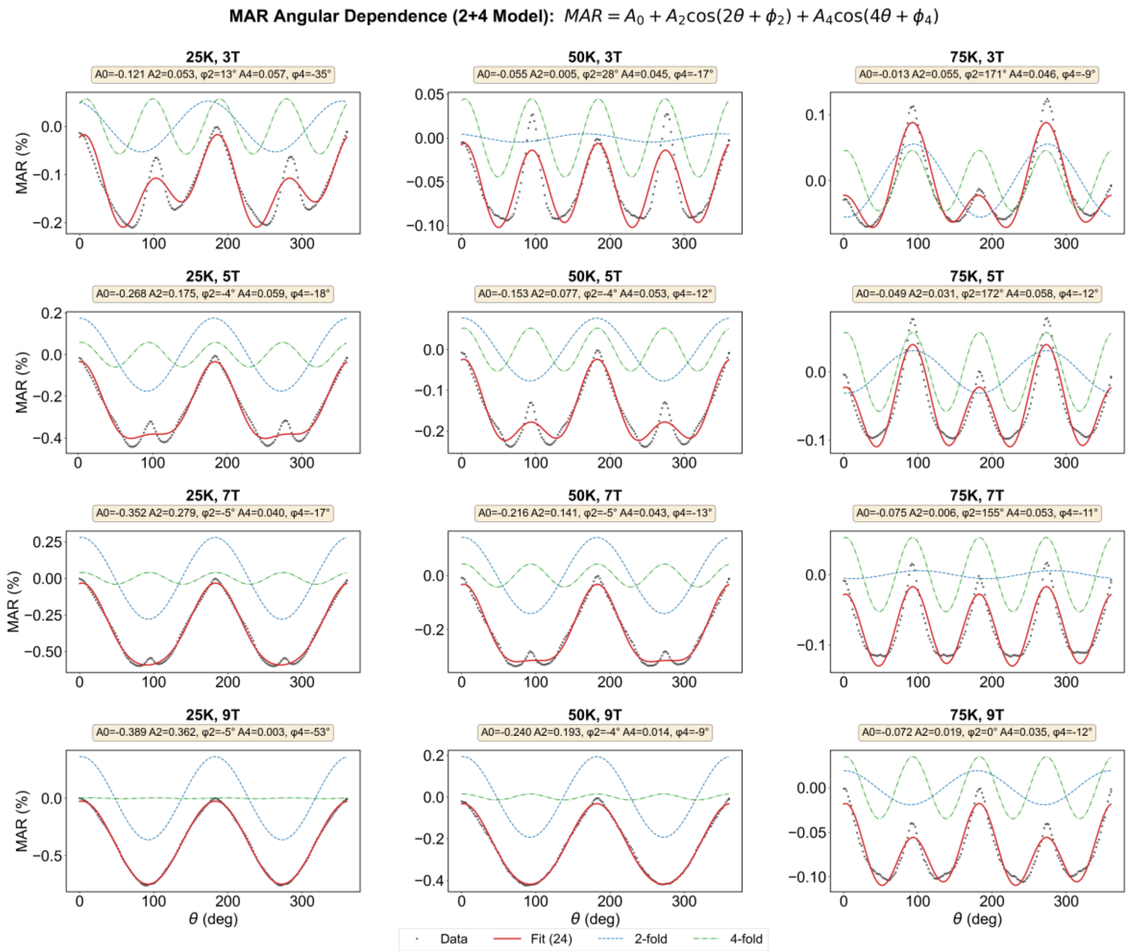

Supplementary Figure 9. Two-component harmonic decomposition (two-fold and four-fold) of the MAR results for L_9S_6. The model appears to underfit the MAR data, indicating the necessity of a higher-fold component in the MAR results.

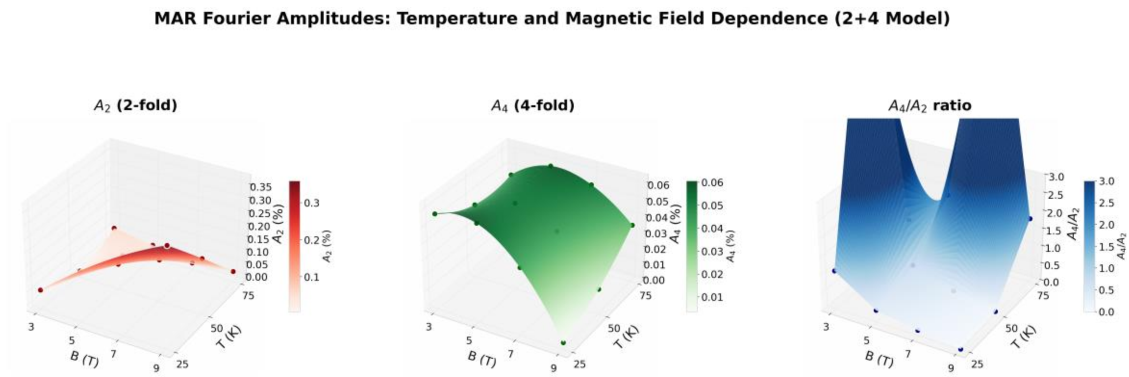

Supplementary Figure 10. The phase diagram of (a) two-fold amplitude A_2, (b) four-fold amplitude A_4 and (c) A_4/A_2 ratio. Though the 2+4 model underfits the MAR data, the A_4/A_2 is still a good order parameter indicating the evolution of the spin reorientation with field and temperature.

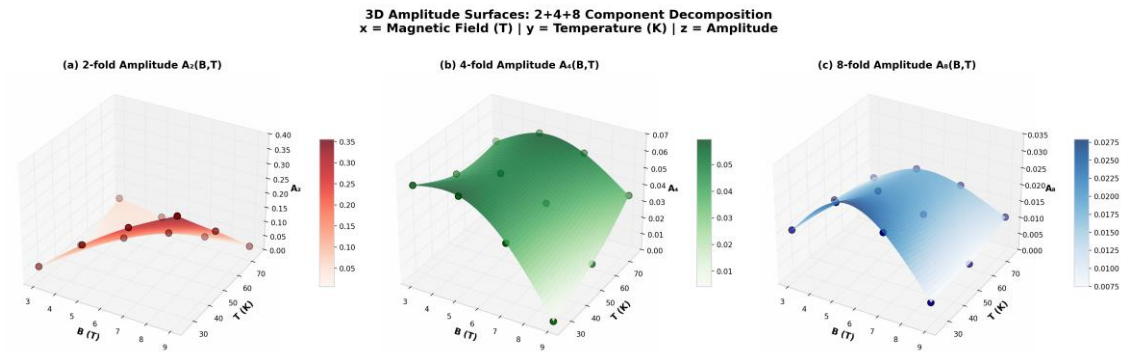

Supplemental Figure S11. 3D plot of the field-temperature evolution of the amplitudes for (a) two-fold, (b) four-fold and (c) eight-fold component in the 2+4+8 harmonic decomposition. The two-fold has strongest amplitude when field is high and temperature is low. The four-fold and eight-fold amplitudes have respective maxima at particular field and temperature, revealing different optimal conditions for each component.

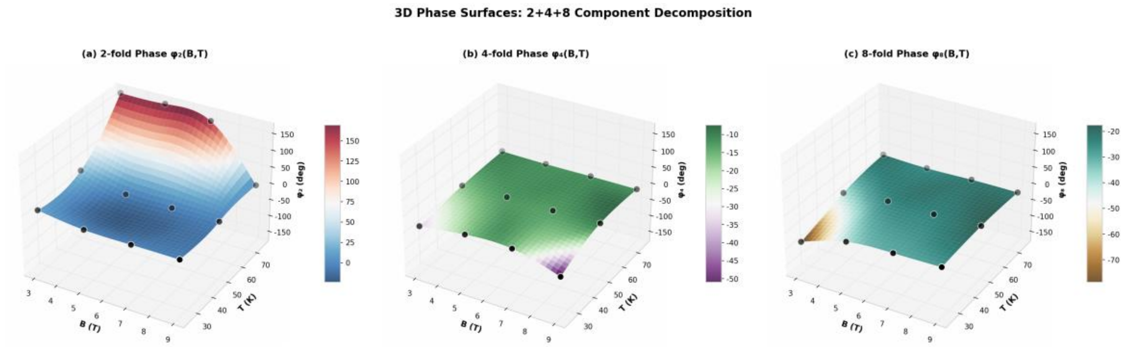

Supplemental Figure S12. 3D plot of the field-temperature evolution of the phases for (a) two-fold, (b) four-fold and (c) eight-fold component in the 2+4+8 harmonic decomposition. The two-fold phase exhibits significant increase with field at 75 K, indicating the presence of complex phase competitions near the Curie temperature of LCO.

Static micromagnetic simulations

The 2D static micromagnetic energy minimization was performed on a 512 nm × 512 nm grid representing the L_9S_6 superlattice geometry (12 bilayers of 9-uc LCO / 6-uc SRO, 72 nm total thickness). The total energy functional includes:

$$E_{\text{eff}} = E_{\text{ex}} + E_{\text{anis}} + E_{\text{DMI}} + E_{\text{demag}} + E_{\text{Zeeman}} + E_{\text{ie}}$$

The effective field is derived from the energy functional via:

$$\mathbf{H}_{\text{eff}} = -\frac{1}{\mu_0 M_s}\frac{\partial E}{\partial \mathbf{m}}$$

- The exchange energy follows a mean-field-like coupling with mean exchange stiffness: $E_{\text{ex}} = -\sum_{\boldsymbol{i}}\sum_{\langle \boldsymbol{j}\rangle} A_{\text{ex}}^{(\boldsymbol{i})}\mathbf{m}_i\mathbf{m}_j\frac{\Delta V}{a^2}$. The effective exchange field $\mathbf{H}_{\text{ex}}^{(i)} = \frac{2A_{\text{ex}}^{(i)}}{\mu_0 M_{\text{s}}^{(i)}}\frac{\text{m}_{i+1}-2\text{m}_i+\text{m}_{i-1}}{a^2}$, where i denotes the stacking sublayer in the superlattice (1.2 nm/sublayer, 3 sublayers for LCO and 2 sublayers for SRO for each LCO/SRO bilayer).

- The anisotropy field follows a standard magnetic interaction form: $E_{\mathrm{anis}} = \sum_i K_{\mathrm{u}}^{(i)}(\mathbf{1} - (\mathbf{m}_i \cdot \hat{\boldsymbol{n}}_i)^{\mathbf{2}})\Delta V$. The effective anisotropic field $\mathbf{H}_{\mathrm{anis}}^{(i)} = \frac{2K_{\mathrm{u}}^{(i)}}{\mu_0 M_{\mathrm{s}}^{(i)}}(\mathbf{m}_i \cdot \hat{\boldsymbol{n}}_i)\hat{\boldsymbol{n}}_i$ with $K_{\mathrm{u}} > 0$ for PMA and $K_{\mathrm{u}} < 0$ for IMA.
- The DMI field follows a reduced 2-component form that assumes the DMI vector $\boldsymbol{D} \parallel \hat{\boldsymbol{z}}$ and only couples in-plane gradients to the out-of-plane magnetization component via first-order finite difference: ($\mathbf{H}_{\mathrm{DMI},x}^{(i)} = \frac{D^{(i)}}{2\mu_0 M_s^{(i)}} \frac{\mathrm{m}_{z,j+1} - \mathrm{m}_{z,j-1}}{dy}$, $\mathbf{H}_{\mathrm{DMI,y}}^{(i)} = \frac{D^{(i)}}{2\mu_0 M_s^{(i)}} \frac{\mathrm{m}_{z,i+1} - \mathrm{m}_{z,i-1}}{dx}$).
- The demagnetizing field is computed via 3D FFT convolution with open-boundary conditions.
- The Zeeman field follows the standard form coupled to external field $\mathbf{H}_{\mathrm{ext}} = B_{\mathrm{ext}}/\mu_0 \hat{\boldsymbol{z}}$.
- The interfacial exchange interaction follows a mean-field-like coupling across the LCO/SRO interface $\mathbf{H}_{\mathrm{ie}}^{(i)} = \frac{J_{\mathrm{ie}}}{\mu_0 M_s^{(i)} dz} \mathbf{m}_{i+1}$ where *i* and *i+1* are the two cells straddling the interface.

The relaxation is achieved by updating a damped alignment $\mathbf{m}^{(n+1)} = \frac{(1-\alpha)\mathbf{m}^n + \alpha \hat{\mathbf{H}}_{\mathrm{eff}}^{(n)}}{\left|(1-\alpha)\mathbf{m}^n + \alpha \hat{\mathbf{H}}_{\mathrm{eff}}^{(n)}\right|}$ with $\alpha = 0.3$ acting as a convergence mixing parameter instead of solving the full Landau-Lifshitz-Gilbert (LLG) dynamics. The system is driven to the nearest local energy minimum accessible from the initial state. The detailed comparison between our all-Python model and a standard GPU-based Mumax3 methods is tabulated in Supplementary Table 1.

Supplementary Table 1. Detailed comparison between our 2D model and the mumax3 solver.

Term	**Our model**	**Mumax3**	**Effect of our model**
Exchange	Mean stiffness	Exact inter-region scaling	Small difference for narrow domain walls
DMI	2-component	Full 3D-tensor	Neglecting vertical DMI between layers
Demagnetizing	Periodic FFT	Approximated open boundary FFT with padding	Fair for strict 2D scheme ($L_{x,y} >> t$)
Interfacial interaction	Explicit mean-field coupling term	Enhanced stiffness at interface instead of a dedicated term	Direct competition between DMI and interfacial exchange interaction, but less accurate for AFM coupling.
Relaxation method	Fixed-point alignment	LLG-dynamics	No precession or time scale

The parameters for the micromagnetic simulation are tabulated as Supplementary Table 2 shown below. The parameters especially the K_{u}(SRO) and M_{s}(SRO) are particularly designed such that the effective saturation field is around 7~9 T, consistent with the MFM observations (Supplemental Figures 2-5). The initial magnetic configuration consists of weakly pinned stripe domains with a period of approximately 128 nm.

Supplementary Table 2. Parameters for SRO layers and LCO layers.

Layer	**Thickness/nm**	**Anisotropy/Jm^{-3}**	**Magnetization/Am^{-1}**
SRO	2.4	$K_{\mathrm{u}} = +4.5\times10^6$ (PMA)	$M_{\mathrm{s}} = 0.8\times10^6$

Layer	Thickness/nm	Anisotropy/Jm^{-3}	Magnetization/Am^{-1}
LCO	3.6	$K_u = -1.0\times10^4$ (IMA)	$M_s = 0.5\times10^6$

Two distinct physical regimes were simulated to compare the effects of DMI versus ferromagnetic interfacial exchange coupling. Case A and Case B represent the DMI-dominated regime and the interfacial-exchange-dominated regimes, respectively. The parameters for each regime are summarized as Supplementary Table 3.

Supplementary Table 3. Parameters for Case A and Case B.

Parameter	Case A	Case B
DMI (SRO)	3.0 mJ/m^2	0.3 mJ/m^2
J_{ie} (interface)	0	+3.0 mJ/m^2 (FM)
Dominant mechanism	Pure DMI	FM interfacial exchange

The table below (Supplementary Table 4) summarizes the SRO magnetization response under varying magnetic fields for both cases. The most striking difference occurs at 5 T, where Case A shows a magnetization of 0.36 while Case B remains near zero at 0.07 — a difference factor of approximately 5×.

Supplementary Table 4. Simulated magnetization results for Case A and Case B.

Physical Quantity	Case A ($J_{ie} = 0$)	Case B ($J_{ie} = +3.0$)
0 T SRO $\langle m_z \rangle$	–0.0003 (≈ 0)	–0.0008 (≈ 0)
0 T SRO tilt angle	5.5°	3.8°
0 T negative fraction	50.2%	50.3%
3 T SRO $\langle m_z \rangle$	0.0357	0.0266
5 T SRO $\langle m_z \rangle$	0.3640	0.0712
7 T SRO $\langle m_z \rangle$	0.9999 (saturated)	0.9434 (not saturated)
9 T SRO $\langle m_z \rangle$	1.0000	1.0000

Main observations and interpretations are reported in the main text and this section here serves as a supportive material.

Two-channel AHE modelling for all samples

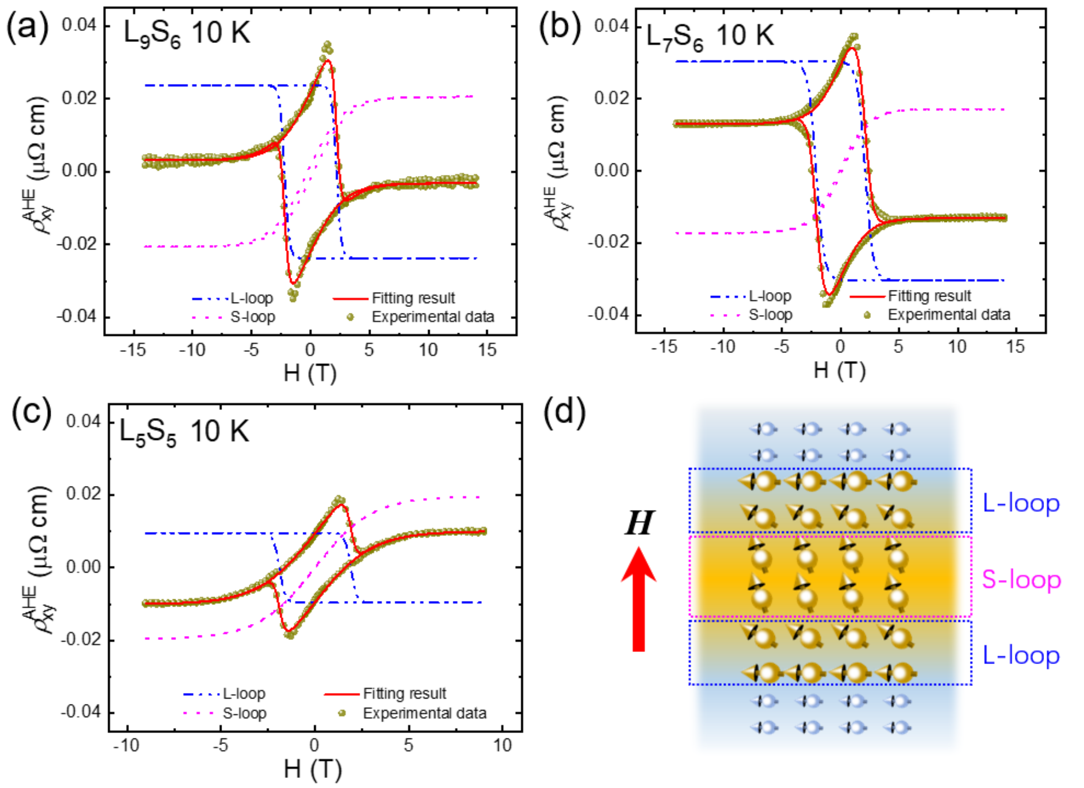

Supplementary Figure 13. Hall resistivity fitted by two-channel AHE model for (a) L_9S_6, (b) L_7S_6 and (c) L_5S_5, respectively, with a largely coercive "L-loop" representing the interfacial robust ferromagnetic coupling, and a weakly coercive "S-loop" representing the bulk ferromagnetism in the SRO layers as denoted in (d).

Transport properties for all samples

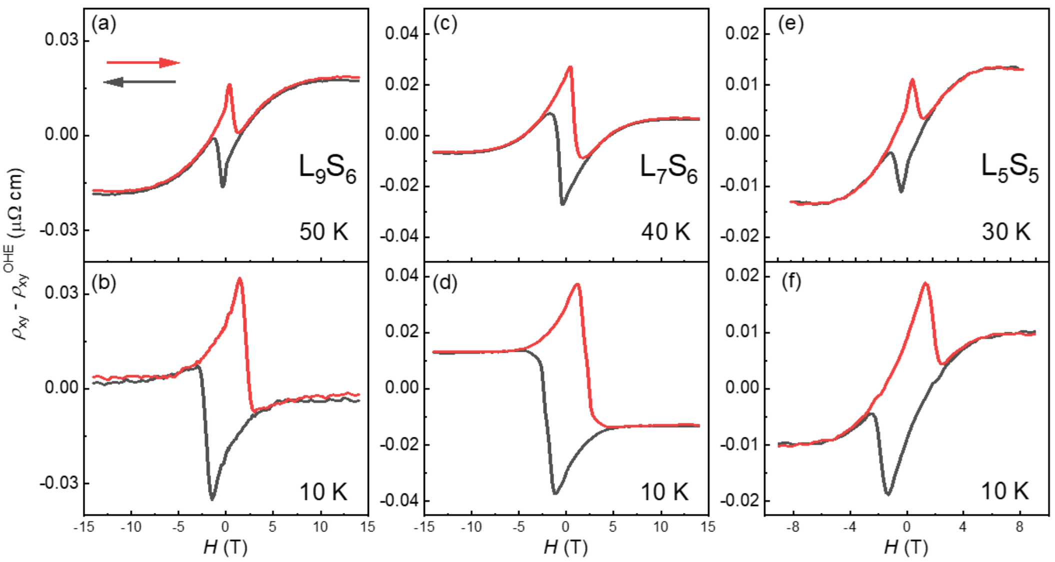

Supplementary Figure 14. Hall resistivity as a function of field at various temperatures. Red and grey colors represent different scanning directions.

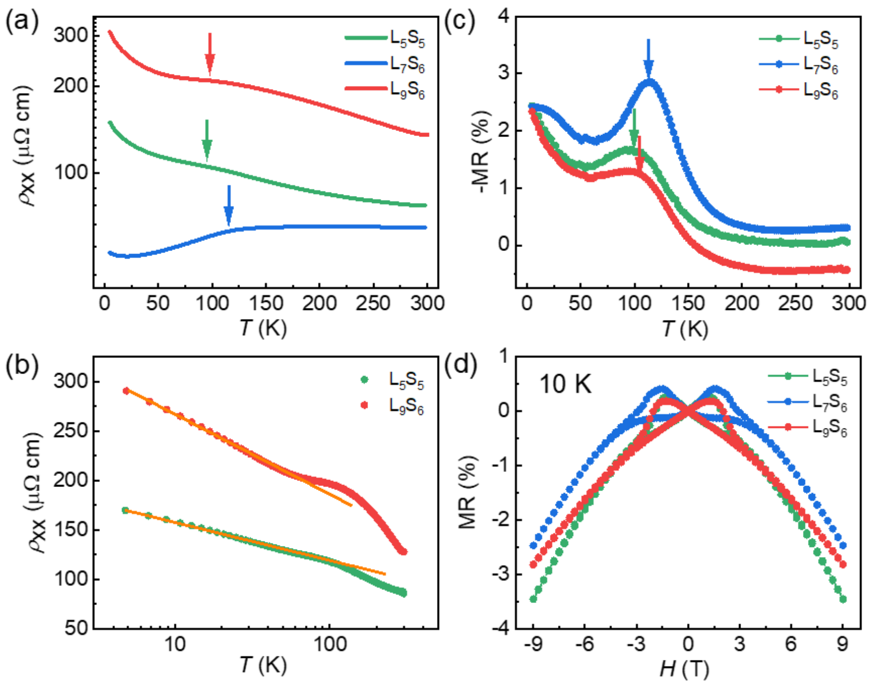

Supplementary Figure 15. (a) Temperature dependence of the longitudinal resistivity at zero field. A slope change in each curve is denoted by green, blue and reds arrows for L_5S_5, L_7S_6 and L_9S_6, respectively. (b) Zoom-in plot for L_9S_6 and L_5S_5 of (a). (c) Temperature dependence of the negative percent change of the magneto-resistivity with respect to zero field ($-MR = [\rho(0) - \rho(H)] / \rho(0)$) at 7 T. (d) MR as a function of field strength at 10 K.

Magnetization results for all samples

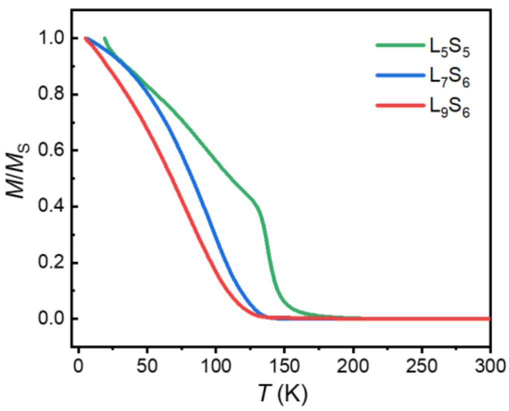

Supplementary Figure 16. Normalized magnetizations as a function of temperature for all samples.